PCCP

PAPER

Cite this: *Phys. Chem. Chem. Phys.*, 2016, **18**, 30040

Energetics of native defects in anatase TiO_2: a hybrid density functional study†

Adisak Boonchun,[ab] Pakpoom Reunchan[a] and Naoto Umezawa*[bc]

Received 22nd August 2016,
Accepted 9th October 2016

DOI: 10.1039/c6cp05798e

www.rsc.org/pccp

The energetics and electronic structures of native defects in anatase TiO_2 are comprehensively studied using hybrid density functional calculations. We demonstrate that oxygen vacancies (V_O) and titanium interstitials (Ti_i) act as shallow donors, and can form at substantial concentrations, giving rise to free electrons with carrier densities from 10^{11} to 10^{19} cm^{-3} under oxygen-rich and oxygen-poor conditions, respectively. The titanium vacancies (V_{Ti}), identified as deep acceptors and induced hole carriers, are incapable of fully compensating for the free electrons originating from the donor-type defects at any oxygen chemical potential. Even under extreme oxygen-rich conditions, the Fermi level, which is determined from the charge neutrality condition among charge defects, electron and hole carriers, is located 2.34 eV above the valence band maximum, indicating that p-type conductivity can never be realized under any growth conditions without external doping. This is consistent with common observations of intrinsic n-type conductivity of TiO_2. At a typical annealing temperature and under a typical oxygen partial pressure, the carrier concentration is found to be approximately 5×10^{13} cm^{-3}.

1 Introduction

TiO_2 is a technologically important wide-bandgap semiconductor with applications as a transparent conducting oxide (TCO),[1,2] in photocatalysis[3] and solar cells,[4,5] and as a ferromagnetic wide-bandgap oxide.[6,7] TiO_2 exists as three polymorphs: rutile, anatase, and brookite. Anatase has been the favored phase for nanopowdered photocatalytic applications due to its higher activity than rutile,[8,9] although nanostructures like nanorods and nanotubes with rutile structures have also been synthesized.[10,11] The anatase phase is important for TCO applications possibly due to its smaller electron-effective mass than rutile. There are several reports on doping for the n-type conductivity of anatase TiO_2-based TCO,[1,12–15] and reports on p-type conductivity are very rare. The photoexcitation of electron–hole pairs in pristine TiO_2 requires relatively high photon energy and occurs only under ultraviolet light. In practice, reduced TiO_2 can absorb photon in the visible light region according to the abundance of trivalent Ti (Ti^{3+}).[16,17] Reduced TiO_2 also exhibits n-type conductivity,[18–20] the origin of which was proposed to be donor-type defects like oxygen vacancies (V_O) and titanium interstitials (Ti_i).[18] First-principles calculations based on density functional theory (DFT) have been established as an important tool for understanding and acquiring knowledge of native defects in general.

Native defects in anatase TiO_2 were previously studied using local-density approximation (LDA) and generalized gradient approximation (GGA).[21,22] However, recent studies revealed that self-interaction correction and its repercussions for polaronic effects are important for discussing the electronic and magnetic properties of native defects in metal oxides.[23] The approximation methods that include some of the essential correlation- or orbital-dependent effects, such as LDA+U (or GGA+U) and hybrid functionals, are more insightful for understanding and gaining knowledge of native defects. Morgan and Watson[24] reported a GGA+U study of the transition levels and single-particle levels of donor- and acceptor-type native defects in anatase TiO_2. They suggested that V_O and Ti_i are deep donors that donate two and four electrons, respectively, whereas V_{Ti} is a deep acceptor generating four holes.

Since the Heyd–Scuseria–Ernzerhof (HSE) hybrid functional[25] yields a better description of the bandgap, it should also be useful for accurate estimations of the defect levels in semiconductors and metal oxides. Janotti *et al.*[26] performed HSE hybrid functional calculations on rutile TiO_2 and showed that oxygen vacancies are stable in their positively charged states V_O^{2+} for any Fermi energy within the bandgap, indicating that they are shallow donors. Recently, P. Deák *et al.*[27] also studied oxygen vacancies and carrier self-trapping in anatase and rutile TiO_2 using HSE06,[25] and showed that oxygen vacancies are

[a] *Department of Physics, Faculty of Science, Kasetsart University, Bangkok 10900, Thailand*
[b] *International Center for Materials Nanoarchitectonics (MANA), National Institute for Materials Science, 1-1 Namiki, Tsukuba, Ibaraki 305-0044, Japan*
[c] *Center for Materials research by Information Integration (CMI²), National Institute for Materials Science, 1-2-1 Sengen, Tsukuba, Ibaraki 305-0047, Japan. E-mail: umezawa.naoto@nims.go.jp*

† Electronic supplementary information (ESI) available: The optimized structure of native defects in anatase TiO_2. See DOI: 10.1039/c6cp05798e

shallow donors in both anatase and rutile phases. Finazzi *et al.*[28] demonstrated using GGA+U (with U = 4 eV) or B3LYP hybrid functionals that charge-neutral oxygen vacancies in anatase TiO_2 create defect states at 1 eV below the conduction band. Recently, P. Deák *et al.*[29] found that oxygen vacancies and titanium interstitials are both shallow donors by using HSE06. The single-particle Kohn–Sham levels associated with Ti interstitials were also investigated using spin-polarized hybrid DFT.[28] Malashevich *et al.*[30] studied oxygen vacancies in the rutile structure using DFT+GW, and found that the transition level of charged states from +2 to +1, ε(+2/+1), is higher than that from +2 to neutral, ε(+2/0), showing negative U behavior. From their estimation it is found that ε(+2/0) lies 2.8 eV above the VBM.

These theoretical studies mainly focused on the identification of defect levels and the validation of computational results obtained from the different methods. However the Fermi level position and carrier concentrations in intrinsic anatase TiO_2 have not been quantitatively estimated. Moreover, the origin of the n-type conductivity is still controversial and a theoretical study based on accurate computational methods is required. In this study, we employ the HSE06 hybrid functional, which was proven to be reliable for defect calculations in TiO_2,[31] to conduct a comprehensive study for the energetics of native defects in anatase TiO_2 and to estimate carrier concentration under a given oxygen partial pressure. Since the antisite defects (TiO and O_{Ti}) have high formation energies,[21] they are not considered in the present study. The native point defects examined in this study are V_{Ti}, V_O, Ti_i and O interstitials (O_i) in anatase TiO_2.

2 Computational method

Our study is based on DFT calculations using the HSE hybrid functional.[25] The calculations were performed using the VASP code[32] with the projector-augmented wave (PAW) method.[33] We used a well-converged energy cut-off of 400 eV for the projector-augmented plane waves. In conventional unit cells, the Brillouin zone is expressed using 5 × 5 × 5 Monkhorst–Pack meshes.

For Ti, $3s^2 3p^6 4s^2 3d^2$ states were treated as valence states. In the HSE approach, the Coulomb potential in the exchange energy is divided into short-range and long-range parts with a screening length of 10 Å. In the short-range part, the non-local Hartree–Fock (HF) exchange is mixed with the Perdew, Burke, and Ernzerhof (PBE) GGA exchange energy.[34] The long-range part and the correlation potential are represented by the PBE functional.

We used the standard HF mixing α = 0.25 which is suitable for the satisfaction of generalized Koopmans' theorem[35] in both anatase and rutile TiO_2.[31] The geometry relaxation was performed for a cell volume and shape, as well as for atomic positions of a 12-atom conventional cell, until the residual force is less than 0.02 eV $Å^{-1}$. Our calculated lattice constants are a = 3.760 Å and c = 9.621 Å, which were close to other HSE06-reported constants of a = 3.755 Å and c = 9.561 Å,[31] and experimental results: a = 3.782 Å and c = 9.502 Å.[36]

Our calculated indirect bandgap is 3.73 eV for the transition from the valence band maximum (VBM) near the M point (0.425, 0.425, 0) to the conduction band minimum (CBM) at Γ. Although we attempted to use the same cut-off energy and valence electron configuration potentials as were used in previous HSE06 calculations,[31] we somehow still obtained a larger bandgap, which is accidentally equal to the adiabatic bandgap of G_0W_0 calculations (3.73 eV).[37] Note that, both HSE06 and quasi-particle G_0W_0 bandgaps are higher than the experimentally measured optical bandgap (3.42 eV)[38]

For defect calculations, we extended the conventional cell by 3 × 3 × 1 to produce a 108-atom supercell and introduced a defect in the supercell. K-points were sampled at a Monkhorst–Pack special 1 × 1 × 1 mesh for the Brillouin zone integration of the supercell. Calculations for charged states were also performed for each defect with neutralizing background charge. The charged states considered here are (+2, +1, 0) for V_O, (+4, +3, +2, +1, 0) for Ti_i, (−4, −3, −2, −1, 0) for V_{Ti} and (+2, +1, 0, −1, −2) for O_i. The effects of spin polarization were included for all charged states. Relaxations were performed for atomic positions with a fixed cell volume until the residual force is less than 0.02 eV $Å^{-1}$.

Fictitious interactions between the charged defect with its images in neighboring cells and with the homogeneous background charge were removed using the scheme proposed by Makov and Payne.[39] Normally, the quadrupole term in the Makov and Payne correction can be approximated to about one-third of the monopole term for cubic supercells as reported by Lany and Zunger.[40] Since the supercell used in this study is non-cubic, the non-cubic adjustment[41] has been used to correct the quadrupole term in Makov and Payne correction. The dielectric constant is needed in the Makov and Payne correction. From HSE calculations for dielectric constants of anatase TiO_2,[42] the average value of 46.23 was used in the correction.

To ensure the convergence of the cell size, we carried out the formation energy calculations of oxygen vacancies in neutral charged states with a larger supercell size of 216 atoms, *i.e.* 3 × 3 × 2 extension of the conventional cell. We found that the formation energy of neutral charge V_O is changed only by 0.075 eV as the cell size increased from 108 to 216 atoms. The relaxed geometries for all defects examined are shown in the ESI.†

To identify the dominant type of native defect, we compared the stabilities of Ti_i, V_{Ti}, V_O and O_i. The formation energy of a native defect D with charged state q is defined as

$$E_f(D^q) = E_{tot}(D^q) - E_{tot}(TiO_2) - n_i\mu_i + q(\varepsilon_F + E_V), \quad (1)$$

where $E_{tot}(D^q)$ is the total energy of the cell with defect D in charged state q. $E_{tot}(TiO_2)$ is the total energy of the cell without defects and n_i is the number of atoms of a species i (Ti or O) that have been added to ($n_i > 0$) or removed from ($n_i < 0$) the supercell. ε_F is the Fermi energy that ranged over the bandgap. Note that ε_F is the energy of the electron reservoir with respect to the VBM, E_V, which is corrected in a defect-containing supercell by aligning the electrostatic potential in a region far away from the defect site with the corresponding potential in a perfect crystal.

Finally, μ_i is a chemical potential representing the energy for defect D that is taken from the reservoir. We reference chemical

potentials $\tilde{\mu}_i$ to the energy per atom of the isolated elemental phase: $\tilde{\mu}_O = \mu_O - \frac{1}{2}E_{tot}[O_2]$ and $\tilde{\mu}_{Ti} = \mu_{Ti} - E_{tot}[Ti_{bulk}]$. These reference energies are given by our DFT calculations for a total energy of bulk Ti per formula unit (−9.46 eV) and a half of the total energy of an isolated O_2 molecule (−8.55 eV).

The chemical potential is a variable but it must satisfy the thermodynamic equilibrium condition of TiO_2, $\tilde{\mu}_{Ti} + 2\tilde{\mu}_O = \Delta H_f(TiO_2)$, where $\Delta H_f(TiO_2)$ is the formation enthalpy of TiO_2. At the oxygen-rich limit ($\tilde{\mu}_O = 0$), the chemical potential of Ti is given by $\tilde{\mu}_{Ti} = \Delta H_f(TiO_2)$. At the Ti-rich limit, $\tilde{\mu}_{Ti}$ is bound by the formation of Ti_2O_3, $2\tilde{\mu}_{Ti} + 3\tilde{\mu}_O < \Delta H_f(Ti_2O_3)$.[21] The formation enthalpies estimated using the HSE approach are $\Delta H_f(TiO_2)$ = −9.756 eV and $\Delta H_f(Ti_2O_3)$ = −15.493 eV which are in good agreement with the previous report.[43,44] After all, the chemical potential settings ($\tilde{\mu}_{Ti}$, $\tilde{\mu}_O$) corresponding to Ti-rich (O-poor) and O-rich (Ti-poor) are (−1.72, −4.02) and (−9.76, 0) in eV, respectively.

In addition to the extreme chemical potential conditions (Ti-rich and O-rich), we consider an intermediate oxygen chemical potential corresponding to a realistic growth condition during the annealing of anatase TiO_2. The oxygen chemical potential is a function of temperature and oxygen partial pressure, as described in ref. 45

$$\tilde{\mu}_O(T, p) = \tilde{\mu}_O(T, p_0) + \tfrac{1}{2}k_B T \ln(p/p_0), \quad (2)$$

where $\tilde{\mu}_O(T, p_0)$ is the oxygen chemical potential at the standard pressure p_0 = 1 atm, k_B is Boltzmann's constant, and T is the temperature in Kelvin. The typical annealing temperature used in the growth of anatase TiO_2 is 400–550 °C[1,2,46] and the typical oxygen partial pressure is 10^{-4}–10^{-5} Torr.[47] We therefore chose an annealing temperature of 550 °C and an oxygen partial pressure of 10^{-5} Torr, which corresponds to ($\tilde{\mu}_{Ti}$, $\tilde{\mu}_O$) = (−6.70, −1.52) in eV.

The thermodynamic transition levels are given by the Fermi energy at which the formation energies of the two charged states are equal [ESI†]:

$$\varepsilon_D(q/q') = \frac{E_f(D^q; \varepsilon_F = 0) - E_f(D^{q'}; \varepsilon_F = 0)}{q' - q}. \quad (3)$$

The thermodynamic transition is represented by kinks in the plots of formation energy as a function of Fermi energy. Note that ε_F ranges over the bandgap and references to the VBM.

The concentration of a native defect D with charge q, $c(D^q)$, is related to its formation energy E_f through the equation

$$c(D^q) = N_{sites}/(1 + \exp^{E_f(D^q)/k_B T}), \quad (4)$$

where N_{sites} is the number of possible lattice sites per unit volume (V_{cell}) at which the defect can be formed.

The hole concentration (p) and electron concentration (n) can be expressed by the following equations:[48]

$$n = 2\left(\frac{m_e k_B T}{2\pi\hbar^2}\right)^{3/2} \exp^{(\varepsilon_F - E_g)/k_B T}, \quad (5)$$

$$p = 2\left(\frac{m_h k_B T}{2\pi\hbar^2}\right)^{3/2} \exp^{-\varepsilon_F/k_B T}, \quad (6)$$

where m_e and m_h are the electron- and hole-effective masses, respectively, and E_g is the bandgap. The charge neutrality is satisfied when the summation of donor and electron carrier concentrations equals the acceptor and hole carrier concentrations

$$\sum_i q_i c_i(D^q) + p - n = 0. \quad (7)$$

The index i represents the donor- or acceptor-type defect. In our calculations, the experimental hole-effective mass of $0.8m_0$ and electron effective mass of $1.2m_0$ were used.[49]

3 Results

Fig. 1 shows the formation energies obtained from our hybrid DFT calculations as a function of the Fermi energy. The lower and upper limits of the Fermi energy correspond to the VBM and the CBM, respectively. The slope of each line reflects the stable charged state of each defect, *e.g.* V_O^{2+} is stable over the other charged states of V_O in the entire range of Fermi energies. The transition levels $\varepsilon(q/q')$ corresponding to each defect are listed in Table 1, some of which are also shown as filled circles in Fig. 1.

Under Ti-rich conditions (Fig. 1(a)), Ti_i^{4+} has the lowest formation energy among the defects examined over a wide range of Fermi energies. However, the predominance overturns at a higher Fermi energy, *i.e.* the formation energy of V_O^{2+} is slightly lower than that of Ti_i^{4+} near the CBM. On the other hand, the formation energy of V_{Ti}^{4-} is higher than those of V_O^{2+} and Ti_i^{4+} at any Fermi level, indicating that hole carriers induced by the acceptor-type defect (V_{Ti}^{4-}) are incapable of compensating for electrons induced by the donor-type defects (V_O^{2+} and Ti_i^{4+}). In fact, the Fermi level determined by the charge neutrality condition at a typical annealing temperature of 550 °C is pinned at the CBM under the Ti-rich conditions according to our following analysis. The pinned Fermi levels are denoted as up-pointing arrows in Fig. 1 for each $\tilde{\mu}_O$ condition. When the transition level is above the CBM, the Fermi level is considered pinned at the CBM. At the oxygen-rich limit, the formation energy of V_{Ti}^{4-} is lowered and the carrier compensation effect is more pronounced, as observed in the downward shift of the Fermi level, although it is still higher than the VBM by 2.34 eV and cannot reach p-type conductivity (Fig. 1(c)). Here, the formation of V_O^{2+} is still favored compared to Ti_i^{4+} at the pinned Fermi level. Under an intermediate μ_O corresponding to experimental growth conditions (oxygen partial pressure 10^{-5} Torr at 550 °C),[47] the Fermi level is located at 2.72 eV. Again, V_O^{2+} predominates over Ti_i^{4+} at the pinned Fermi level (Fig. 1(b)), and therefore is considered the major source of electron carriers. Thus, V_O^{2+} is the predominant donor-type defect under any $\tilde{\mu}_O$ condition.

Ti_i is stable in the form of the quadruple charged state. The nearest oxygen neighbor along the vertical c-axis relaxes inward by 23.6% in Ti_i while the two nearest-neighbor oxygen atoms on the basal axis relax outward by only 0.37%. The optimized structure of Ti_i is shown in Fig. S1(b) in the ESI.† Most of the thermodynamic transition levels for Ti_i shown in Table 1 are located above the CBM, reflecting that it is a shallow donor.

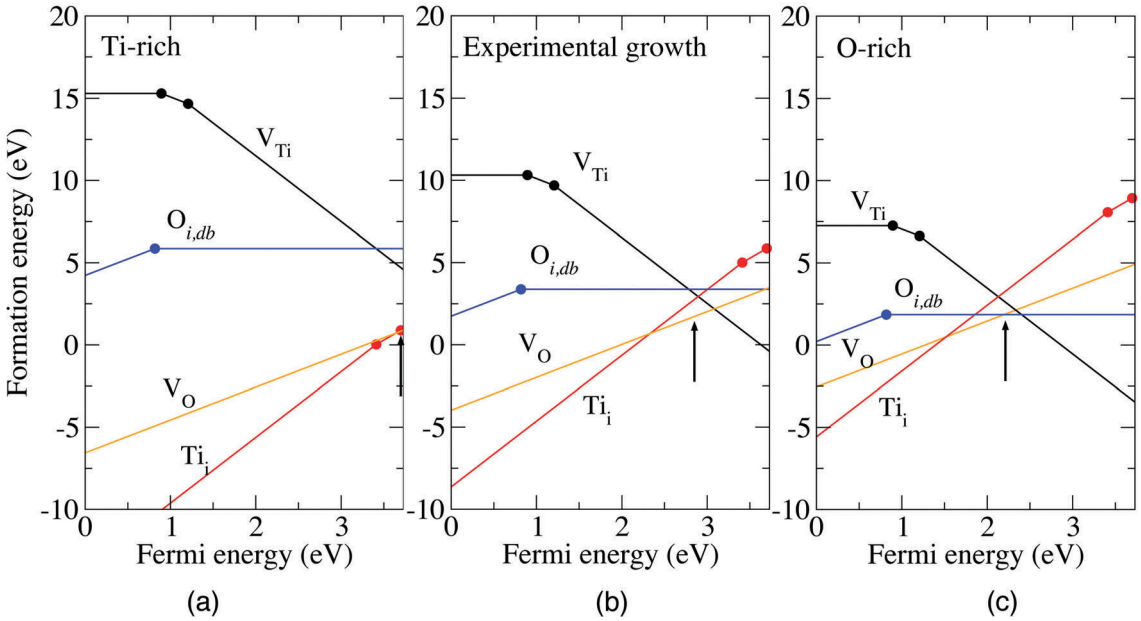

Fig. 1 Defect formation energies as a function of Fermi energy under (a) Ti-rich, (b) experimental growth, and (c) O-rich conditions. The up-pointing arrow indicates the Fermi level determined by the charge neutrality condition at 550 °C.

V_O is stable in the doubly charged state. There are three nearest-neighbor Ti atoms around V_O. In the neutrally charged state, one Ti nearest-neighbor relaxes outwards by 8.39% while the other two relax outwards by 2.80%. The optimized structure of V_O is shown in Fig. S1(c) in the ESI.† The transition levels $\varepsilon(+2/+)$ and $\varepsilon(+2/0)$ (not shown in Fig. 1) are located above the CBM, which is consistent with previous reports using the HSE approach for rutile[26] and anatase.[29] Note that in our HSE06 calculation, we used the low-frequency limit of the dielectric constant in Lany–Zunger charge correction[40] while P. Deák *et al.*[29] applied a high-frequency dielectric constant in Lany–Zunger charge correction. Interestingly, our calculation and the calculation of P. Deák *et al.*[29] yield qualitatively consistent results in terms of the point that both V_O and Ti_i exhibit the nature of shallow donors. By contrast, DFT+*U* predicted that they are deep donors.[24,43]

O_i atoms are more stable in a dumbbell configuration ($O_{i,db}$) than in an octahedral configuration ($O_{i,oct}$), in the form of peroxide ions at oxygen lattice sites. All the neighboring Ti atoms relax outward only slightly. The optimized structure of $O_{i,db}$ is shown in Fig. S1(d) in the ESI.† Substitutional O_2 has a bond length of 1.44 Å in the neutral charged state, which is slightly longer than that in an isolated O_2 molecule (1.21 Å). The transition level $\varepsilon(+2/0)$ is located 0.81 eV above the VBM, indicating that it is a deep donor. The detailed analysis of O_i has been studied by Paul Erhart *et al.*[50]

The V_{Ti} defect changes its charged state from neutral to −2 to −4 as the Fermi energy increases, as shown in Fig. 1. The thermodynamic transition levels are located in the band gap: $\varepsilon(0/-2) = 0.89$ and $\varepsilon(-2/-4) = 1.21$ eV, which indicates that V_{Ti} is a deep acceptor. Recently, Chen and Dawson showed that V_{Ti} is not stable with respect to the complex defect $V_{Ti} + 2V_O + O_2$ for the Fermi level less than 1.37 eV by using HSE06.[51] The formation energy of this complex is very high and does not contribute in our charge neutrality calculation. In anatase, the axial bond lengths are longer than the equatorial bond lengths. The nearest-neighbor oxygen atoms in the basal plane containing V_{Ti}^{4-} relax outwards by 4.6%, whereas the nearest-neighbor oxygen atoms in the axial direction relax outwards by 20%. The optimized structure of V_{Ti} is shown in Fig. S1(e) in the ESI.†

Fig. 2(a) shows defect concentrations as a function of oxygen chemical potential or oxygen partial pressure at 550 °C. Note that eqn (7) is satisfied for each oxygen chemical potential in the plots shown in Fig. 2. It is clear that the concentration of V_O^{2+} is higher than that of Ti_i^{4+} for any oxygen chemical potential, while the concentration of V_{Ti}^{4-} is limited. It should be noted that we considered only point defects for the estimation of carrier concentrations and effects of complex or line defects are not taken into account. Fig. 2b shows the Fermi level determined through the charge neutrality condition (eqn (7)) for each oxygen chemical potential. The Fermi level is elevated as the O_2 partial

Table 1 The transition level $\varepsilon(q, q')$ all in eV reference to the VBM

Defect	q, q'	$\varepsilon(q, q')$
V_O	+2/+	3.92
	+2/0	3.82
Ti_i	+4/+3	3.41
	+3/+2	3.70
	+2/+1	3.82
	+1/0	4.01
V_{Ti}	0/−2	0.89
	−2/−4	1.21
O_i	+2/0	0.81

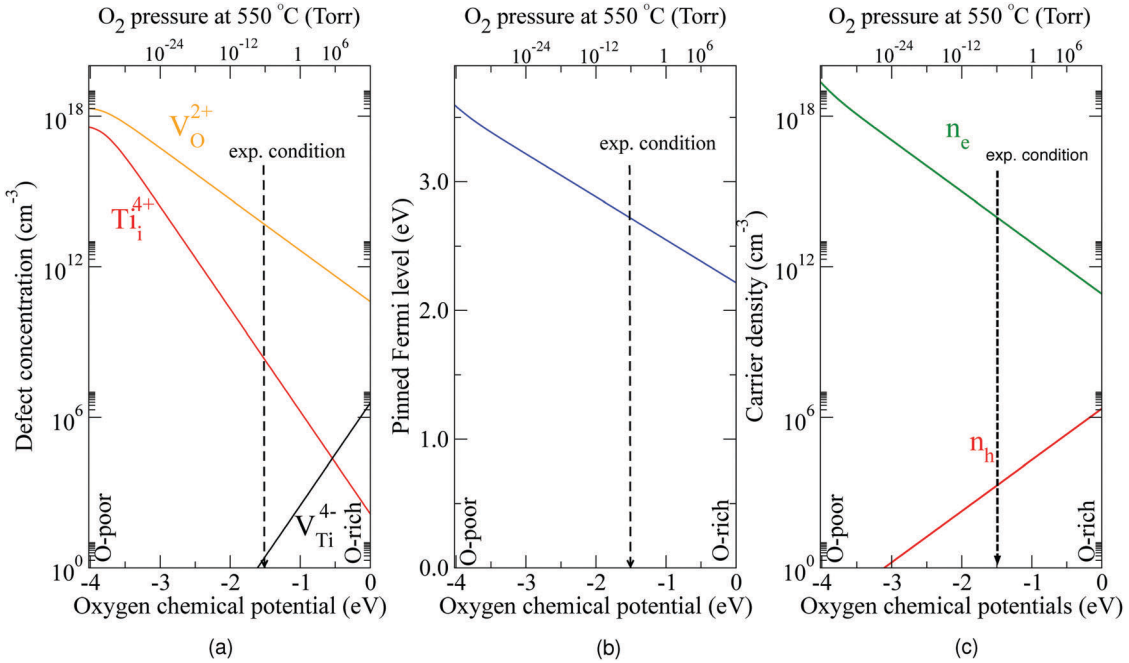

Fig. 2 (a) The defect concentration, (b) pinned Fermi energy and (c) carrier concentration (electrons n_e and holes n_h) as a function of oxygen chemical potentials. The down-pointing arrow with the vertical dashed line indicates the oxygen chemical potential, −1.52 eV, corresponding to the experimental condition at the annealing temperature of 550 °C and under an oxygen partial pressure of 10^{-5} Torr.

pressure decreases, consistent with experimental observations. The lowest Fermi level (2.34 eV) is reached under the O-rich condition, although it is still much higher than the VBM. This indicates that the intrinsic p-type conductivity can never be realized under any equilibrium growth condition. In fact, holes are minority carriers in anatase TiO_2, as shown in Fig. 2(c), in which the carrier densities of electrons and holes defined by eqn (5) and (6) for each oxygen chemical potential are compared. As observed from Fig. 2c, the electron density increases with decreasing oxygen chemical potential and reaches a very high density (2.32×10^{19} cm^{-3}) under extremely O-poor conditions, which is in a similar order to the experimental result.[13] The result is also consistent with the common observation that electrical conductivity increases with decreasing oxygen partial pressure.[52]

From these results, we conclude that V_O^{2+} is the major source of n-type conductivity of anatase TiO_2. This result does not exclude the existence of Ti_i^{4+} because we found that a significant amount of Ti_i^{4+} is present, especially under O-poor conditions (Fig. 2(a)).

Multiple electron paramagnetic resonance (EPR) signals associated with trivalent titanium ions have been observed for reduced anatase TiO_2.[53] The previous theory suggested that the origin of trivalent titanium is either oxygen vacancies or titanium interstitials.[17] Our estimation suggests that the concentration of $[V_O^{1+}]$ is two orders of magnitude higher than that of $[Ti_i^{3+}]$. Thus, we suggest that the strong EPR signal is associated with trivalent titanium originates from $[V_O^{1+}]$.

The single-particle Kohn–Sham levels associated with the neutral and charged defects of Ti_i and V_O are shown in Fig. 3. For charged defects, both spin-up and spin-down channels are depicted along with spin-un-polarized cases. The correction is also necessary for single-particle Kohn–Sham levels according to previous studies.[54–56] The horizontal dashed line represents an adiabatic computational band gap of 3.73 eV. In Ti_i, the occupied Kohn–Sham levels of the ionized cases are all located lower than those in the neutral case, consistent with the common observation for single ions, *i.e.* the second-ionization energy is higher than the first-ionization energy. In contrast, the occupied state of V_O^{1+} lies higher than that of V_O^0, because of the large atomic relaxations around positively charged oxygen vacancies. As discussed earlier, the Ti ions that are nearest neighbors to V_O^{1+} are relaxed outwards, leading to the upward shift of the single-particle levels. We found that this effect is more pronounced in our case than in previous studies for rutile TiO_2 using 20% of mixing parameter in HSE.[26]

Thomas *et al.*[57] used X-ray photoelectron spectroscopy (XPS) to find that the electron energy loss is 0.9 eV below the CBM in rutile and 1.1 eV in anatase. We found that the Kohn–Sham levels of V_O^0 and Ti_i^{3+} are 2.89 and 2.70 eV above the VBM. If we consider the adiabatic computational band gap of 3.73 eV, the defect levels of V_O^0 and Ti_i^{3+} are 0.84 and 1.03 eV below the CBM. The vertical ionization energy measured from XPS is more likely to be originating from Ti_i^{3+}. These species can also be the source of the blue color observed in reduced anatase TiO_2.[58,59] Note that these occupied charged states are not the predominant form of the defects according to our formation energy analysis (Fig. 1) and their concentrations are therefore limited.

4 Conclusions

In summary, due to the failure of the self-interaction error of local and semi-local density functional approximations and

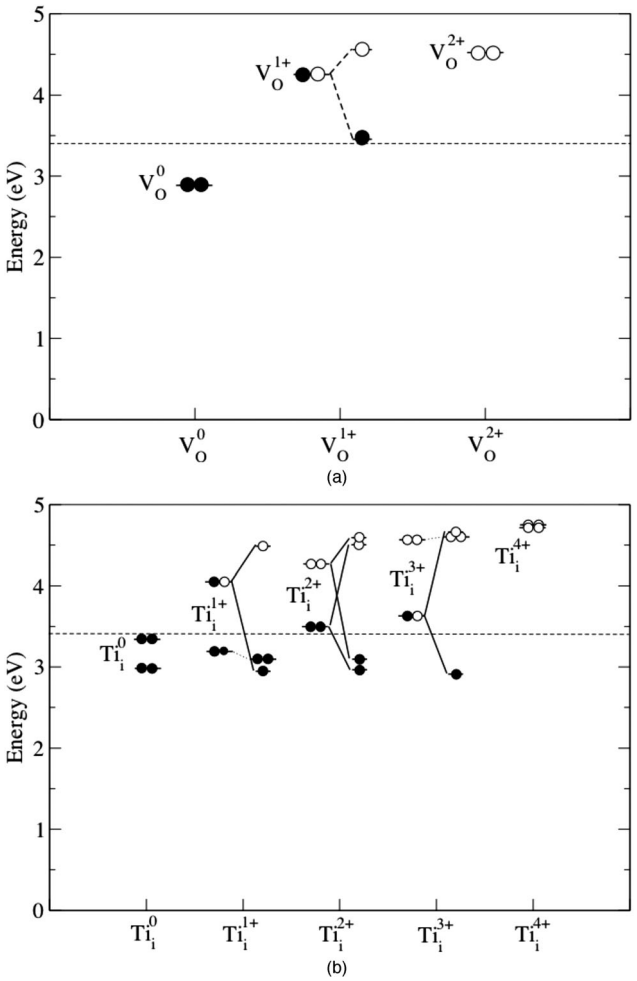

Fig. 3 Calculated position of the single-particle state of (a) V_O and (b) Ti_i in both non-spin-polarized calculations (left side) and spin-polarized calculations (right side). The calculated adiabatic band gap is represented by dashed lines.

their repercussions for polaronic defects, we performed calculations using the Heyd–Scuseria–Ernzerhof (HSE) hybrid functional[25] to gain more insight into the electronic properties of native defects and their likelihood of formation under various growth conditions. The native point defects examined in this study are Ti vacancies (V_{Ti}), O vacancies (V_O), Ti interstitials (Ti_i) and O interstitials (O_i). Our calculations showed that V_O and Ti_i act as double and quadruple shallow donors, respectively. These defects give rise to high carrier concentrations of free electrons from 10^{11} to 10^{19} cm^{-3} under oxygen-rich to oxygen-poor conditions, respectively. On the other hand, V_{Ti} behaves as a deep acceptor and can alternatively be described as a donor compensating defect. We found that hole carriers of these donor-compensating defects are not capable of fully compensating for the free electrons originating from the donor-type defects for any oxygen chemical potential. Under extremely oxygen-rich conditions, the Fermi level is located 2.34 eV above the valence band maximum, indicating that p-type conductivity can never be realized in reality. Our result is consistent with common observations of intrinsic n-type conductivity of TiO_2. At a typical annealing temperature of 550 °C and under an oxygen partial pressure of 10^{-5} Torr, the calculated pinned Fermi level is estimated to be 2.72 eV above the valence band maximum. Note that Fermi-level pinning reported in this work is legitimate only if there are no electrically active impurities. In reality, the absence of active impurities barely occurs in available anatase samples. Under any growth conditions, the concentration of V_O was higher than that of Ti_i; therefore, V_O is considered the major source of the n-type conductivity in anatase.

Our calculated concentration of V_O^{1+} is higher than that of Ti_i^{3+}. Consequently, the origin of trivalent titanium ions on reduced TiO_2, observed by EPR measurements, is possibly associated with V_O^{1+}. In addition, the calculated Kohn–Sham levels associate with V_O and Ti_i revealing that vertical ionization measured from XPS originates from Ti_i^{3+}.

Acknowledgements

N. U. was partly supported by the Japan Science and Technology (JST) Agency, Precursory Research for Embryonic Science and Technology (PRESTO) and the Core Research for Evolutional Science and Technology (CREST) programs. A. B. was supported by Thailand Research Fund for New Researcher (TRG5780264) and Kasetsart University Research and Development Institute (KURDI). P. R. was supported by KURDI. We wish to thank High-performance computing facilities of King Mongkut's University of Technology Thonburi (KMUTT, Thailand) for their hospitality. We acknowledge A. Janotti, S. Limpijumnong and J. B. Varley for fruitful discussions. We also thank J. Ye and H. Abe for their support.

References

1 Y. Furubayashi, T. Hitosugi, Y. Yamamoto, K. Inaba, G. Kinoda, Y. Hirose, T. Shimada and T. Hasegawa, *Appl. Phys. Lett.*, 2005, **86**, 252101.
2 T. Hitosugi, Y. Furubayashi, A. Ueda, K. Itabashi, K. Inaba, Y. Hirose, G. Kinoda, Y. Yamamoto, T. Shimada and T. Hasegawa, *Jpn. J. Appl. Phys.*, 2005, **44**, L1063–L1065.
3 A. Fujishima and K. Honda, *Nature*, 1972, **238**, 37–38.
4 M. Gratzel, *Nature*, 2001, **414**, 338–344.
5 U. Bach, D. Lupo, P. Comte, J. E. Moser, F. Weissörtel, J. Salbeck, H. Spreitzer and M. Grätzel, *Nature*, 1998, **395**, 583–585.
6 Y. Matsumoto, M. Murakami, T. Shono, T. Hasegawa, T. Fukumura, M. Kawasaki, P. Ahmet, T. Chikyow, S.-y. Koshihara and H. Koinuma, *Science*, 2001, **291**, 854–856.
7 L.-H. Ye and A. J. Freeman, *Phys. Rev. B: Condens. Matter Mater. Phys.*, 2006, **73**, 081304.
8 T. Sumita, T. Yamaki, S. Yamamoto and A. Miyashita, *Appl. Surf. Sci.*, 2002, **200**, 21–26.
9 T. Watanabe, A. Nakajima, R. Wang, M. Minabe, S. Koizumi, A. Fujishima and K. Hashimoto, *Thin Solid Films*, 1999, **351**, 260–263.
10 Y. Li, X.-Y. Yang, Y. Feng, Z.-Y. Yuan and B.-L. Su, *Crit. Rev. Solid State Mater. Sci.*, 2012, **37**, 1–74.

11 X. Chen and S. S. Mao, *Chem. Rev.*, 2007, **107**, 2891–2959.
12 H. Tang, K. Prasad, R. Sanjins, P. E. Schmid and F. Lvy, *J. Appl. Phys.*, 1994, **75**, 2042–2047.
13 L. Forro, O. Chauvet, D. Emin, L. Zuppiroli, H. Berger and F. Lvy, *J. Appl. Phys.*, 1994, **75**, 633–635.
14 Y. Furubayashi, T. Hitosugi, Y. Yamamoto, K. Inaba, G. Kinoda, Y. Hirose, T. Shimada and T. Hasegawa, *Appl. Phys. Lett.*, 2005, **86**, 252101.
15 T. Hitosugi, Y. Furubayashi, A. Ueda, K. Itabashi, K. Inaba, Y. Hirose, G. Kinoda, Y. Yamamoto, T. Shimada and T. Hasegawa, *Jpn. J. Appl. Phys.*, 2005, **44**, L1063.
16 R. F. Howe and M. Gratzel, *J. Phys. Chem.*, 1985, **89**, 4495–4499.
17 C. Di Valentin, G. Pacchioni and A. Selloni, *J. Phys. Chem. C*, 2009, **113**, 20543–20552.
18 U. Diebold, *Surf. Sci. Rep.*, 2003, **48**, 53–229.
19 S. A. Bilmes, P. Mandelbaum, F. Alvarez and N. M. Victoria, *J. Phys. Chem. B*, 2000, **104**, 9851–9858.
20 M. K. Nowotny, T. Bak and J. Nowotny, *J. Phys. Chem. B*, 2006, **110**, 16270–16282.
21 S. Na-Phattalung, M. F. Smith, K. Kim, M.-H. Du, S.-H. Wei, S. B. Zhang and S. Limpijumnong, *Phys. Rev. B: Condens. Matter Mater. Phys.*, 2006, **73**, 125205.
22 J. Osorio-Guill'en, S. Lany and A. Zunger, *Phys. Rev. Lett.*, 2008, **100**, 036601.
23 W. R. L. Lambrecht, *Phys. Status Solidi B*, 2011, **248**, 1547–1558.
24 B. J. Morgan and G. W. Watson, *Phys. Rev. B: Condens. Matter Mater. Phys.*, 2009, **80**, 233102.
25 J. Heyd, G. E. Scuseria and M. Ernzerhof, *J. Chem. Phys.*, 2006, **124**, 219906.
26 A. Janotti, J. B. Varley, P. Rinke, N. Umezawa, G. Kresse and C. G. Van de Walle, *Phys. Rev. B: Condens. Matter Mater. Phys.*, 2010, **81**, 085212.
27 P. Deák, B. Aradi and T. Frauenheim, *Phys. Rev. B: Condens. Matter Mater. Phys.*, 2012, **86**, 195206.
28 E. Finazzi, C. Di Valentin and G. Pacchioni, *J. Phys. Chem. C*, 2009, **113**, 3382–3385.
29 P. Deák, B. Aradi and T. Frauenheim, *Phys. Rev. B: Condens. Matter Mater. Phys.*, 2015, **92**, 045204.
30 A. Malashevich, M. Jain and S. G. Louie, *Phys. Rev. B: Condens. Matter Mater. Phys.*, 2014, **89**, 075205.
31 P. Deák, B. Aradi and T. Frauenheim, *Phys. Rev. B: Condens. Matter Mater. Phys.*, 2011, **83**, 155207.
32 G. Kresse and J. Furthmüller, *Comput. Mater. Sci.*, 1996, **6**, 15–50.
33 P. E. Blöchl, *Phys. Rev. B: Condens. Matter Mater. Phys.*, 1994, **50**, 17953–17979.
34 J. P. Perdew, K. Burke and M. Ernzerhof, *Phys. Rev. Lett.*, 1996, **77**, 3865–3868.
35 S. Lany and A. Zunger, *Phys. Rev. B: Condens. Matter Mater. Phys.*, 2009, **80**, 085202.
36 J. K. Burdett, T. Hughbanks, G. J. Miller, J. W. Richardson and J. V. Smith, *J. Am. Chem. Soc.*, 1987, **109**, 3639–3646.
37 M. Landmann, E. Rauls and W. G. Schmidt, *J. Phys.: Condens. Matter*, 2012, **24**, 195503.
38 H. Tang, F. Lévy, H. Berger and P. E. Schmid, *Phys. Rev. B: Condens. Matter Mater. Phys.*, 1995, **52**, 7771–7774.
39 G. Makov and M. C. Payne, *Phys. Rev. B: Condens. Matter Mater. Phys.*, 1995, **51**, 4014–4022.
40 S. Lany and A. Zunger, *Phys. Rev. B: Condens. Matter Mater. Phys.*, 2008, **78**, 235104.
41 H.-P. Komsa, T. T. Rantala and A. Pasquarello, *Phys. Rev. B: Condens. Matter Mater. Phys.*, 2012, **86**, 045112.
42 B. Lee, C.-k. Lee, C. S. Hwang and S. Han, *Curr. Appl. Phys.*, 2011, **11**, S293–S296.
43 N. Umezawa and J. Ye, *Phys. Chem. Chem. Phys.*, 2012, **14**, 5924–5934.
44 C. B. A. O. Kubaschewski and P. J. Spencer, *Materials Thermochemistry*, Pergamon Press, Oxford, 6th edn, 1993.
45 K. Reuter and M. Scheffler, *Phys. Rev. B: Condens. Matter Mater. Phys.*, 2001, **65**, 035406.
46 H. Irie, Y. Watanabe and K. Hashimoto, *J. Phys. Chem. B*, 2003, **107**, 5483–5486.
47 Y. Hirose, N. Yamada, S. Nakao, T. Hitosugi, T. Shimada and T. Hasegawa, *Phys. Rev. B: Condens. Matter Mater. Phys.*, 2009, **79**, 165108.
48 M. Grundmann, *The physics of semiconductors: an introduction including devices and nanophysics*, Springer Science & Business Media, 2006.
49 Y.-X. Weng, Y.-Q. Wang, J. B. Asbury, H. N. Ghosh and T. Lian, *J. Phys. Chem. B*, 2000, **104**, 93–104.
50 P. Erhart, A. Klein and K. Albe, *Phys. Rev. B: Condens. Matter Mater. Phys.*, 2005, **72**, 085213.
51 H. Chen and J. A. Dawson, *Phys. Rev. Appl.*, 2015, **3**, 064011.
52 A. Weibel, R. Bouchet and P. Knauth, *Solid State Ionics*, 2006, **177**, 229–236.
53 S. Livraghi, M. Chiesa, M. C. Paganini and E. Giamello, *J. Phys. Chem. C*, 2011, **115**, 25413–25421.
54 S. E. Taylor and F. Bruneval, *Phys. Rev. B: Condens. Matter Mater. Phys.*, 2011, **84**, 075155.
55 I. Dabo, B. Kozinsky, N. E. Singh-Miller and N. Marzari, *Phys. Rev. B: Condens. Matter Mater. Phys.*, 2008, **77**, 115139.
56 S. Lany and A. Zunger, *Phys. Rev. B: Condens. Matter Mater. Phys.*, 2010, **81**, 113201.
57 A. G. Thomas, W. R. Flavell, A. K. Mallick, A. R. Kumarasinghe, D. Tsoutsou, N. Khan, C. Chatwin, S. Rayner, G. C. Smith, R. L. Stockbauer, S. Warren, T. K. Johal, S. Patel, D. Holland, A. Taleb and F. Wiame, *Phys. Rev. B: Condens. Matter Mater. Phys.*, 2007, **75**, 035105.
58 T. Sekiya, K. Ichimura, M. Igarashi and S. Kurita, *J. Phys. Chem. Solids*, 2000, **61**, 1237–1242.
59 T. Sekiya, T. Yagisawa, N. Kamiya, D. Das Mulmi, S. Kurita, Y. Murakami and T. Kodaira, *J. Phys. Soc. Jpn.*, 2004, **73**, 703–710.

